Wind Tunnel Testing of a Complete Formula Student Vehicle

Jaime Rafael Martins Pacheco
jaime.pacheco@tecnico.ulisboa.pt

Instituto Superior Técnico, Universidade de Lisboa, Portugal

June 2022

Abstract

Formula Student teams are putting a great effort into aerodynamics as it is an important feature to enhance car performance. They focus on designing the best aerodynamic concept through numerical simulations. Before being manufactured, the final concept should pass an experimental test phase which is usually overlooked but essential to build trust in the numerical results. This work presents a first evaluation of the numerical methods adopted by the Formula Student Técnico team. The objective is to verify the quality of CFD results by using verification (quantification of numerical errors) and validation (quantification of modelling errors). First, the numerical errors were estimated through a mesh convergence analysis. Then, to validate the numerical models, a 1/3 scale model of the latest prototype FST10e was built and tested. The wind tunnel tests were performed not only to obtain measurements of quantities of interest (lift, drag and pitching moment) but also to evaluate the physics of the CFD simulations by using flow visualization techniques. First, the wind tunnel facility was characterized by taking speed measurements inside its test section. The data was then used to perform an initial evaluation of the numerical simulations. Finally, the model was tested in six different configurations, in which aerodynamic forces were recorded. In general, the qualitative evaluation of the results revealed that the numerical simulations captured the experimental trends and the sensitivity of each coefficient studied. Also, wool tufts were used as a flow visualization technique, which enhanced the agreement between the numerical simulations and the wind tunnel testing. Despite capturing the wind tunnel results trends and physics, the CFD simulations still need time investment and more testing to provide accurate data. However, they proved to be useful in assessing how the geometry changes affect the aerodynamic performance of the car.

Keywords: Validation, Wind tunnel, Experimental tests, Numerical simulation, Formula Student, Aerodynamic performance

1. Introduction

In the late 1960s, aerodynamic devices were introduced in the motorsport industry. In that early phase, experimental tests were the only option to develop aerodynamic designs since computational capability was almost non-existent. Nevertheless, even with the substantial computational improvement, computational fluid dynamics (CFD) simulations still do not have the capability to entirely replace experimental tests. CFD simulations are still not completely reliable on their own, it acts as a complement to wind tunnel testing. However, the later is the only reliable alternative to obtain experimental data that allows the assessment of the CFD modelling error. It recreates on track conditions in an controlled environment.

Usually in motorsport, wind tunnel tests uses racecar models to reduce costs, ease manufacturing and testing and also due to the limited test dimensions.

Formula Student is an international engineering competition where students are challenged to design, manufacture and compete with a single seater formula racecar [1]. Formula Student Técnico (FST) is a team from Instituto Superior Técnico (IST) that competes in both Electric and Driverless categories.

In the last few years, aerodynamics took a fundamental share of the formula student racecar performance. Nowadays, almost every team develops an aerodynamic package to better balance the car and improve its handling. To do so, the downforce (negative lift force) is treated as a priority for the design of the devices, being the drag force considered secondary. It is usual to deal with downforce, drag and pitching moment values as dimensionless numbers, lift, drag and pitching moment coefficients, respectively,

$$C_L = \frac{L}{\frac{1}{2}\rho S v^2}, \quad (1) \qquad C_D = \frac{D}{\frac{1}{2}\rho S v^2}, \quad (2)$$

$$C_M = \frac{M_y}{\frac{1}{2}\rho S v^2 b}, \tag{3}$$

where L is the lift force, D is the drag force, M_y is the pitching moment[1], u is the uniform incoming airflow speed, ρ is the air density, S is the reference area and b the reference chord length.

Until this point, the FST team have developed some knowledge around wind tunnel testing. For the first ever wind tunnel experiment a 40 % scale model of the FST06e rear wing was tested. The tests were made at $10\,\mathrm{m\,s^{-1}}$ which represented a 3.75 lower Reynolds number than what the wing was design for, this was appointed as the main cause for the unexpected results when compared to CFD simulations. Later, a 25% scale model of the complete FST06e was tested (Fig. 1). The low model thickness caused problems related to aeroelastic deformations, thus no conclusive remarks were achievable.

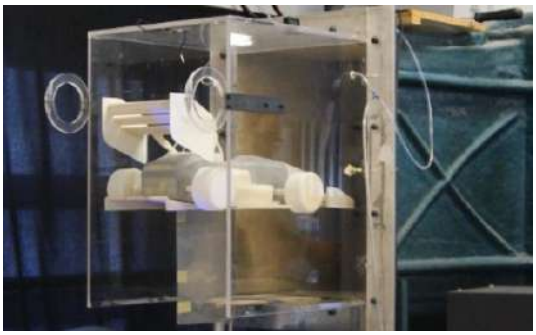

Figure 1: FST06e wind tunnel testing.

In contrast, some Formula Student teams are capable to test their entire car. For instance, Reenteam Uni Stuttgart presented quantitative and qualitative tests that were performed to correlate wind tunnel testing with CFD simulations [2] and AMZ Racing tested its prototype with a procap system that records instantaneous velocity [3].

The FST car aerodynamics have been stagnated for a long time because CFD simulations and rare on track tests (with a lack of instruments) have been the only tools available. As such, the motivation and the major objective for this work is to test the newest racecar of FST to address the quality of its numerical simulations but also the wind tunnel instrumentation and setup will be renovated to make feasible these new experimental works. The deliverables defined to achieve the main goal are:

- Assessment of the numerical error present in the CFD setup;
- Qualitative comparison between the aerodynamic loads of the wind tunnel experiments and the CFD simulations;
- Qualitative comparison between the experimental fluid dynamics (EFD) and CFD simulations physics.

[1] In this work, the pitching moment was calculated around the model-balance support.

2. Wind Tunnel Testing Facilities

The experiments were performed in the closed return aeroacoustic wind tunnel with an open test section (anechoic chamber) at Aerospace Engineering Laboratory at IST. The wind tunnel has an 200 kW motor that rotates a seven blade fan to produce an airflow speed up to $50\,\mathrm{m\,s^{-1}}$. The speed is controlled by the user input of the motor rotations per minute (RPM), which can reach 1500 RPM. However, for safety reasons, the rotational speed is limited to 1000 RPM, producing an airflow of around $43.5\,\mathrm{m\,s^{-1}}$.

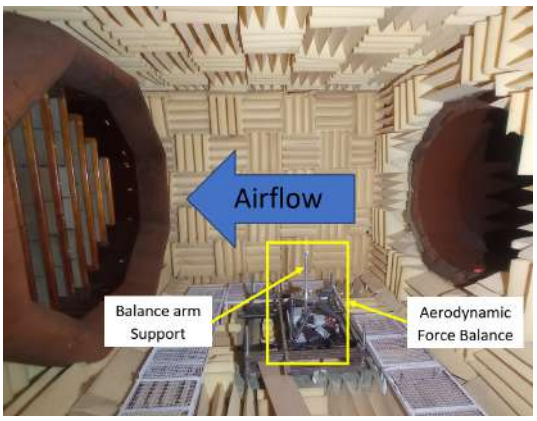

Figure 2: Aeroaccustic wind tunnel test section.

Simulating on road performance can be quite difficult since it is necessary not only to control the environmental conditions but also to measure the forces and moments produced by the model. Usually, the major difficulties are the removal of the wind tunnel boundary layer, the wheel motion reproduction and its contact with the ground. Usually, tufts are the most commonly used techniques to provide diagnostic information relative to the airflow around the object in study [4]. They are attached to the surface with tape or glue, when the air passes through, its direction reproduces the airflow near the surface [5].

As seen in Fig. 2, the facility was not prepared nor had any apparatus for testing a car model. Thus, several steps were taken:

- The wind tunnel facility was upgraded with a structural frame to provide fixed support for the aerodynamic force balance and the model ground;

- The external aerodynamic balance was calibrated to obtain accurate experimental data. A correlation was established between the 6 aerodynamic outputs (F_x - drag, F_y - side force, F_z - lift, M_x - roll, M_y - pitch, M_z - yaw) and the force carried in each bar of the balance;

- Velocity measurements were taken along several sections to characterize the wind tunnel. The measurements enabled the characterization of the turbulence intensity, velocity profiles at several sections and the velocity evolution inside the wind tunnel. The anemometry provided an initial comparison between the experimental and numerical simulations.

3. Mathematical Formulation of the Problem

The numerical simulations intended to recreate the same conditions experimented in the wind tunnel. In this way, the experiments could evaluate the trustworthiness of the numerical simulations. A few numerical studies were performed to evaluate which wind tunnel parts made should be recreated. Due to the limited computational resources, the bare minimum was recreated without compromising the results. The numerical domain was divided in three different stages presented in Fig. 3: nozzle, anechoic chamber test section (where the model was tested) and outlet zone.

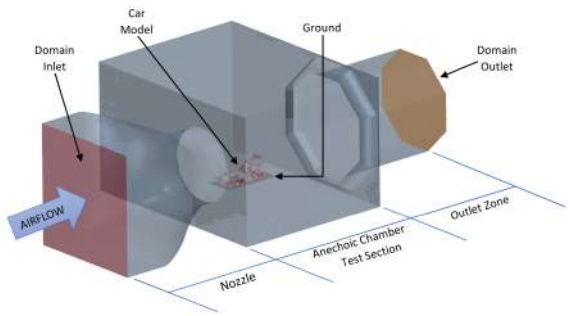

Figure 3: Numerical domain scheme.

The airflow expected while testing the car is characterized by a Reynolds number greater than $Re > 10^6$, and also due to the complex geometries, it is dominated by very small structures. Thus, turbulent flow was the predominant airflow regime. The Reynolds Average Navier Stokes (RANS) equations, particularly the $k-\omega$ SST turbulent eddy viscosity model, are the most appropriate to solve wall bounded flows and present great performance for complex boundary layer flows under adverse pressure gradients [6, 7]. Since eddy viscosity turbulence models are mathematically derived to work with fully turbulent flows, the γ transition model was coupled with the $k-\omega$ SST turbulence model to achieve more realistic transition phenomena [8].

StarCCM+® software was used to perform the CFD simulations. A polyhedral and prism layer meshers were used to discretize the numerical domain, as seen in Fig. 4. Polyhedral cells are constructed from a group of tetrahedral cells that present a successful adaptation to complex geometries, particularly where high refinement is required. The prism layers were constructed targeting a $Wall\ y^+$ smaller than five to ensure that the entire boundary layer airflow was captured.

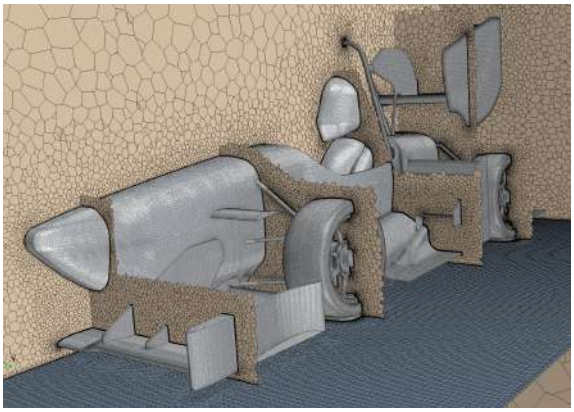

Figure 4: Polyhedral mesh.

Five distinct geometrically similar grids were generated to define the best grid that discretizes the problem. The numerical error was estimated for each grid, the least-squares error estimation method was coupled with the Richard extrapolation method to estimate the exact solution [9] and the numerical uncertainties of the three predominant aerodynamic loads (drag, lift and pitching moment). The convergence analysis showed that mesh number 3 (this mesh has approximately 13.68 million cells and presents a medium level of refinement) represents a good compromise between numerical accuracy and simulation time, it still presents good grid resolution around the car. The lift (C_L) and drag (C_D) coefficients present a numerical error of, respectively, 5.8 %, 4.3 %. Since the pitching moment depends on both lift and drag forces, its error presents the same order of the lift and drag coefficients.

4. Formula Student Model

The preparation of the model geometry began with the FST latest prototype, the FST10e (Fig. 5). External systems that could not be reproduced or did not have a large interference with the aerodynamics of the car were eliminated, such as the cooling system and electrical wires. Other components suffered little changes, for instance, the cockpit was closed, the sharp edges of the wheel assembly were

smoothed and the thickness of the aerodynamics flaps trailing edges was increased to ease manufacturing.

Figure 5: FST10e prototype.

To recreate the conditions of road testing, aerodynamicists rely on similarity parameters [10]. The Reynolds number is a dimensionless number that correlates the ratio between inertial forces and viscous forces,

$$Re = \frac{\rho V l}{\mu}, \tag{4}$$

where V defines the velocity magnitude, l is the reference length and μ is the fluid molecular viscosity. To guarantee Reynolds similarity, assuming equal air density and viscosity, the airspeed must scale with the inverse of the characteristic length, $\frac{V_{model}}{V_{car}} = \frac{l_{car}}{l_{model}}$. The FST10e average speed while competing is approximately $15\,\mathrm{m\,s^{-1}}$. Since the maximum speed of the wind tunnel is around $45\,\mathrm{m\,s^{-1}}$, a 1/3 scale was defined to assure Reynolds similarity. At this speed, the loads on the model and, consequently, on the force balance would be considerably high. To ensure that the balance could cope with the aerodynamic forces, its structural rigidity was verified with an analytical model and an numerical model developed by Oliveira [11].

The 1/3 scale model weighs 9.35 kg and is composed of 149 parts, excluding bolts, nuts, etc. Figure 6 presents an overview of the general components used to assemble the FST10e model.

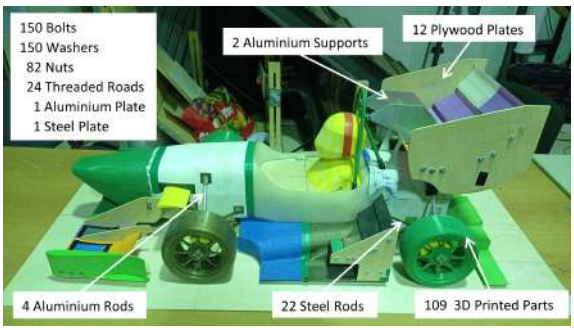

Figure 6: Parts used to assemble the model.

The model is equipped with pressure taps on the front wing, the monocoque nose, the rear wing and inside the lateral diffuser. The model has a hollow interior to offer a place to keep the materials of the pressure sensors without them interfering with the airflow. To provide several testing configurations, the ground clearance of the model can be adjusted and its front and rear wing are adjustable as the real prototype.

The two manufacturing processes predominantly used were 3D printing and Computerized Numerical Control (CNC) machining. The latter was used to manufacture plywood flat components and the rear wing aluminium supports. The remaining components were 3D printed in Polylactic Acid (PLA).

5. Test Configurations

The model was tested at three different ground clearance configurations ($RH1$, $RH2$ and $RH3$) described in Tab. 1. The front and rear ride heights are the ground clearance of the monocoque plane at each axle.

Table 1: Experimental ride heights (RH).

Configuration	$RH1$	$RH2$	$RH3$
Front RH [mm]	10.5	15.4	20.0
Rear RH [mm]	21.5	28.7	35.6
Pitching angle [°]	1.23	1.49	1.75

The first configuration ($RH1$) was tested without bullhorns ($RH1 - NB$) and the third was experimented with two distinct rear wing setups, which were developed for different Formula Student dynamic events, endurance event (high downforce - $RH3$) and acceleration event (recreating a Drag Reduction System (DRS) - $RH3 - DRS$). Figure 7 illustrates the changing components between configurations.

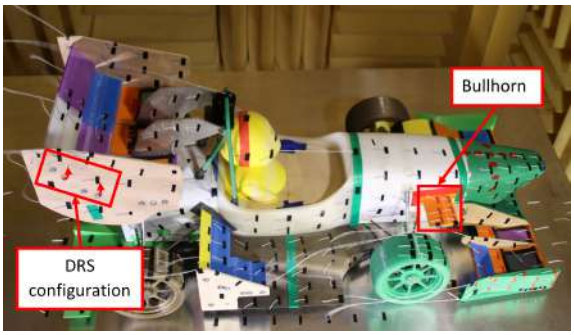

Figure 7: Configuration variation setups.

Initially, the experimental and numerical speed was set to $45\,\mathrm{m\,s^{-1}}$ to meet the flow similarity requirements. However, it was later changed to

$25\,\mathrm{m\,s^{-1}}$ due to problems with the stabilization of the airflow temperature inside the wind tunnel.

6. Flow Visualization

The aerodynamic loads collected by the aerodynamic balance enable the correlation of the wind tunnel data with CFD results. However, since the forces and moments are measured only at a single point, it is impossible to determine the behaviour of each component. Flow visualization can somewhat fill that gap.

It is important to note that phenomena that are smaller than the wool length, like small recirculation zones, might not be captured. Tufts can filter those high frequency perturbations. Moreover, turbulence is a severe unsteady phenomenon, experimental images represent just a moment in time. Thus, some conclusions drawn from the recordings were impossible to represent in figures. In contrast, the numerical simulation presents a time average result. In addition, the airflow presents not only longitudinal but also 3D and mix transverse separations, which are very difficult to trace with tufts.

The following sections present a comparison between the tufts and the surface streamlines simulated numerically. The x axis skin friction on the model surface is presented in two distinct colors: red ($C_{f_x} > 0$) represents the attached airflow and blue ($C_{f_x} < 0$) the separated airflow zones.

The components used to draw the major conclusions from the experimental recordings were the rear wing, tyre and bullhorn and front wing.

6.1. Front Wing

The front wing presented some major discrepancies between the experimental (Fig. 8.(a)) and numerical (Fig. 8.(b)) results.

During the experiments, the tufts only captured some vorticity near the trailing edge of the endplate (marked as zone 2 in Fig. 8.(a)). In contradiction, the numerical simulations captured a large separation zone near the leading edge of the main plane (zone 1 in Fig. 8.(b)). As such, distinct incoming airflows may be responsible for the difference noted. The tufts that were located on the ground surface, in front of the front wing, showed some movement, which means that the ground boundary layer became turbulent even before it reached the front wing. Thus, it can prevent any separation from happening. Also, the numerical domain was not a complete recreation of the experimental apparatus. Under the ground plate, there were several apparatus such us, structures to support the ground in place, the aerodynamic balance and its covers to prevent the airflow to cause undesirable loads, particularly drag. The presence of these components would affect the incoming airflow, changing it. Thus, it is reasonable to assume that the difference marked as number one was caused by both points presented.

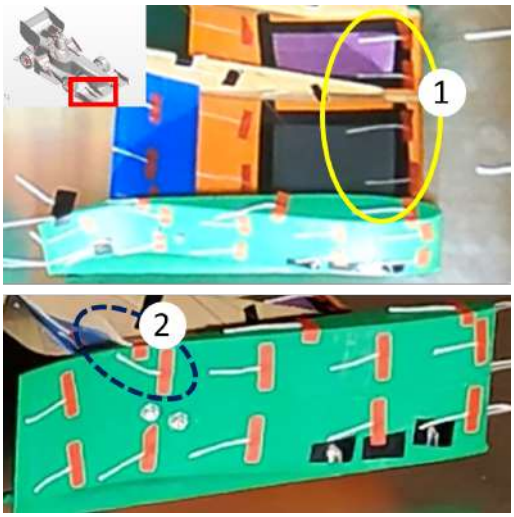

(a) EFD.

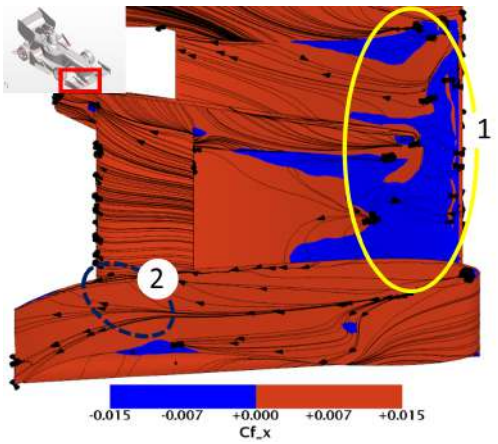

(b) CFD with γ transition model.

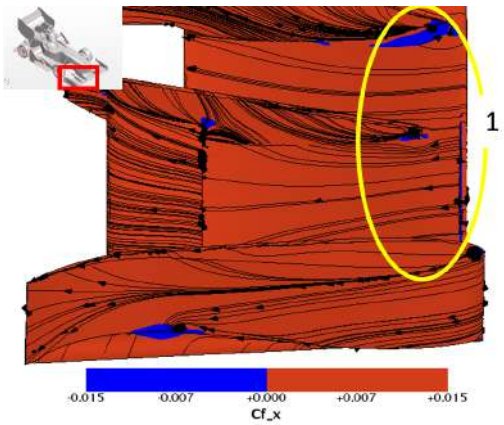

(c) CFD without transition model.

Figure 8: Front wing pressure side flow visualization ($RH1$).

The same geometry was simulated without using a transition model to investigate how it affects the incoming airflow. In this way, the flow is already

turbulent before reaching the front wing. Figure 8.(c) shows that not using a transition model leads to no separation on the front wing pressure surface. Despite being advantageous to predict transition, the γ transition model does not recreate the physics observed inside the wind tunnel.

Regarding the endplate, generally, the surface streamlines reproduce very well the wool tufts behaviour in both simulations. Indeed, an up-wash stream was noticed (zone 2) corresponding to the up-wash created by the front wing flap.

6.2. Rear Wing

Similar to the front wing, the rear wing also presented significant differences between numerical and experimental tests, as illustrated in Fig. 9.

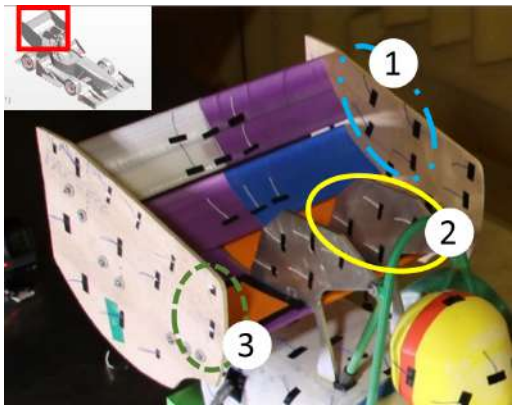

(a) EFD.

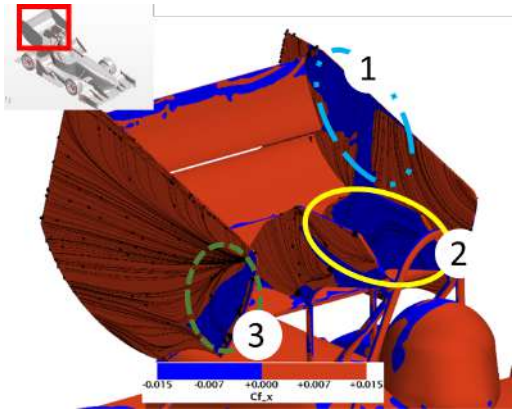

(b) CFD.

Figure 9: Rear wing flow visualization ($RH1$).

The numerical simulations (Fig. 9.(b)) captured three large separation zones: endplate interior (zone 1), rear wing supports interior (zone 2) and endplate exterior (zone 3). However, only zone 3 was reproduced in the experiments. The tufts related to zone 3 show a separation zone near the endplate leading edge (zone 3 in Fig. 9.(a)). The rear wing is located at the rear of the car. Thus, the airflow that reaches it has high turbulence intensity. Also, the wing geometry generates an airflow behaviour with complex combinations of longitudinal and transverse flow separation. For instance, zones 1 and 2 are extremely difficult to analyse using just tufts.

The airflow around the endplates can be complex as well as it is affected by strong vortices. In contrast, the numerical streamlines reproduced the tufts behaviour on the overall surface, as observed on the outer endplate surface.

6.3. DRS study

Regarding the $RH3 - DRS$ configuration, the rear wing flaps are set at a slight negative angle of attack to minimize drag. However, the new angle of attack caused separation on the pressure side of flaps 2 and 3, as illustrated in Fig. 10.(b).

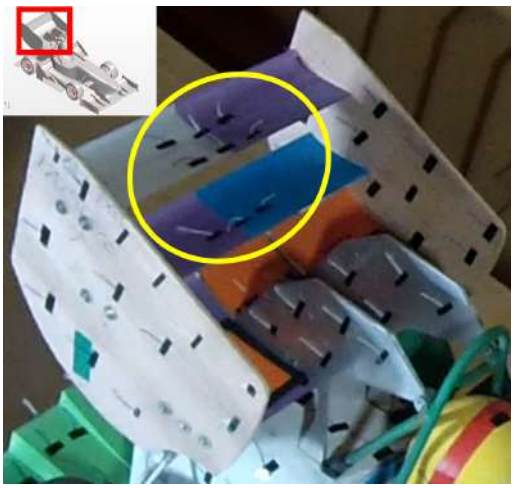

(a) EFD.

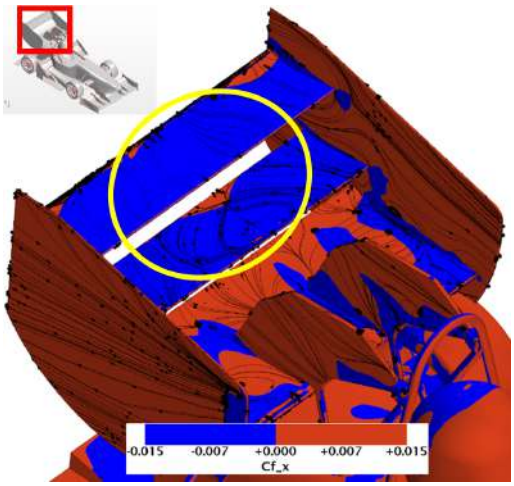

(b) CFD.

Figure 10: Rear wing flow visualization ($RH3 - DRS$).

The tufts located on the flaps pressure side highlighted a high turbulence zone, marked in Fig. 10.(a). The CFD streamlines closely match the flap 2 tufts, yet again, it is hard to identify what is ex-

actly happening on the flaps pressure surfaces using just the tufts visualization method.

Due to the new rear wing configuration, the pressure difference between the inner and outer parts of the endplate is lower than in the last study (Sec. 6.2). Thus, the endplate top vortex has less circulation. The difference in the tufts behaviour highlights that change as well and once again the simulation streamlines match that behaviour.

7. Aerodynamic Loads

The goal of the present work is to perform a qualitative comparison between EFD and CFD. Thus, the quality of the CFD simulations was evaluated by the captured trends.

Some experiments were repeated to overcome the calibration problems. For instance, these experiments will be represented as RHC^* instead of RHC, where C defines the model configuration.

7.1. Bullhorn Study

The first configuration was tested with ($RH1$) and without bullhorns ($RH1 - NB$). Despite generating lift, the bullhorns are supposed to improve the airflow around the car by reducing the upwash generated by the front wing and redirecting the airflow to the side and rear wings, shifting the CoP rearwards. At the same time, they create a vortex to control the tyre wake and to push away the air with low momentum located at the side of the car. Furthermore, it also counters the vortex generated by the rear wing endplate by rotating in the opposite direction. Since the bullhorns performance is directly dependent on the effectiveness of vortices, its position can be hard to establish from numerical simulations. Figure 11 illustrates the relation between the numerical and experimental results for the bullhorn study.

The drag and pitching moment coefficients (Fig. 11.(b) and (c)) present the same trend in the experimental tests as well as in the numerical ones, also the numerical simulations presents almost the same sensitivity as the experimental tests.

The lift and drag coefficients (Fig.11.(a) and (b)) present a small variation. However, the later shows a slight increase with the $RH1 - NB$ configuration in the numerical simulation, which did not represent the behaviour of the wind tunnel tests.

Without bullhorns, the CoP presented higher sensitivity in the numerical simulations, where it shifted forward approximately 7.4% in contrast with the 2.8% in the experimental tests. Indeed, the bullhorns cause a rearwards shift of the CoP.

As a matter of fact, the experimental tests did not provided enough data to prove that the bullhorns are essential to improve the aerodynamics of the car. Despite increasing the lift, it also shifts the CoP rearwards. This might not be worthy as it de-

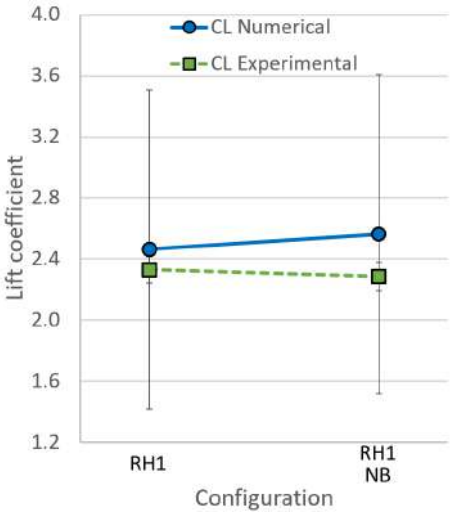

(a) Lift coefficient.

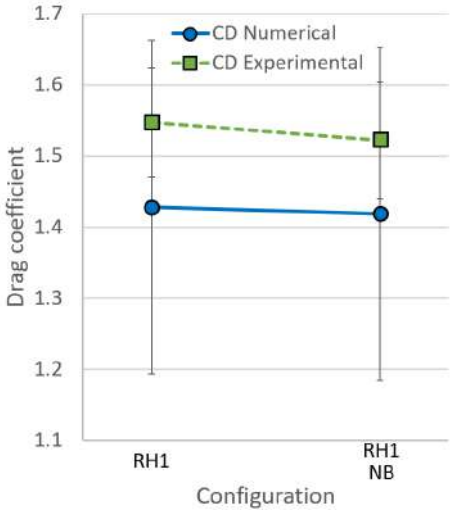

(b) Drag coefficient.

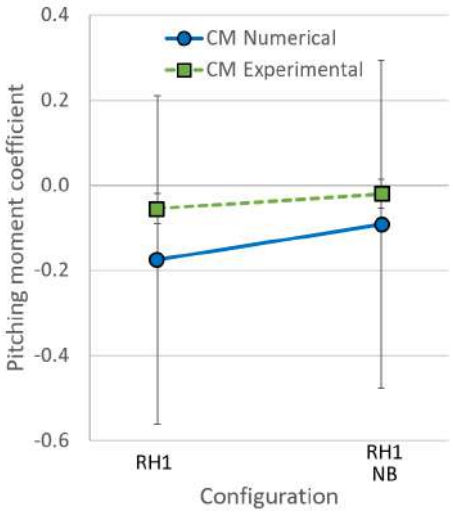

(c) Pitching moment coefficient.

Figure 11: Bullhorn study aerodynamic loads.

teriorates the car handling if the car has already the CoP located behind the CoG, which is the FST10e case.

7.2. Ride Height Study

This study evaluates the sensitivity of the model aerodynamic loads to ground clearance changes. Figure 12 reveals how the lift, drag and pitching moment coefficients behave with the ground clearance.

Experimental tests concluded that the lift coefficient (Fig. 12.(a)) increases with the ground clearance. The lift coefficient curve related to the numerical simulations presented a constant offset for the three configurations. Also, the lift coefficient (Fig. 12.(a)) presents higher sensitivity to lower ride heights. In fact, in both numerical and experimental tests, it experienced a variation around 11% and 3.25%, between $RH1^*$ and $RH2^*$ configurations, and $RH2^*$ and $RH3^*$, respectively.

As expected, the drag coefficient (Fig. 12.(b)) from the experimental and numerical tests followed the increasing behaviour of the lift coefficient. As the model produces more downforce, it also creates more induced drag. During the experimental tests, the $RH2^*$ configuration presented a slight decrease in drag coefficient while the pitching moment coefficient increased. In turn, the numerical simulation does not register this slight drag decrease. This was not true for the $RH1^*$ and $RH3^*$ configurations, for which the numerical results captured the same behaviour of the experimental drag coefficient.

Finally, the variations on the pitching moment coefficient (Fig. 12.(c)) were not captured by the numerical simulations. Generally, the experimental tests present an increase of this coefficient with the increase in ride height.

Taking a further look at the experimental results, the decrease in drag combined with an increase in downforce was not expected. The $RH2^*$ results may be affected due to the car positioning, as a result of a non-zero yaw angle. In this case, the drag force is decomposed into F_x and F_y, affecting the drag and pitching moment coefficients.

7.3. DRS Study

The third configuration ($RH3$) presented a higher pitch angle than the other two. Thus, the rear wing is exposed to cleaner airflow, producing higher aerodynamic loads. The $RH3-DRS$ is an acceleration configuration that aims to reduce the drag force. Figure 13 correlates both ends of the rear wing flaps adjustments.

The three aerodynamic loads and moments studied present the same trend in both the numerical simulations and the experimental tests. Both lift and drag coefficient (Fig. 13.(a) and (b)) decrease in the $RH3-DRS$ configuration.

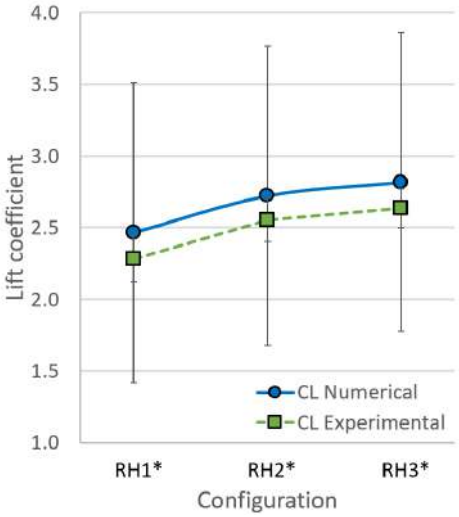

(a) Lift coefficient.

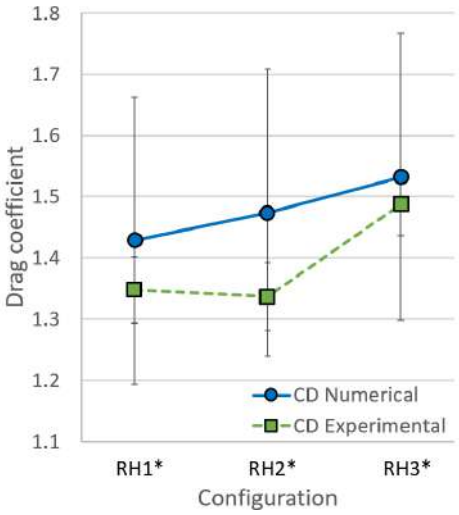

(b) Drag coefficient.

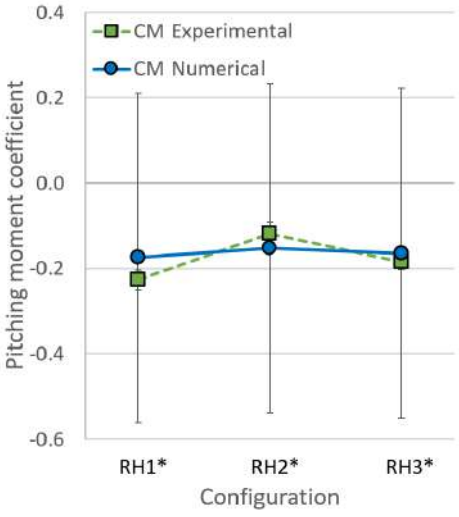

(c) Pitching moment coefficient.

Figure 12: Ride heights study aerodynamic loads.

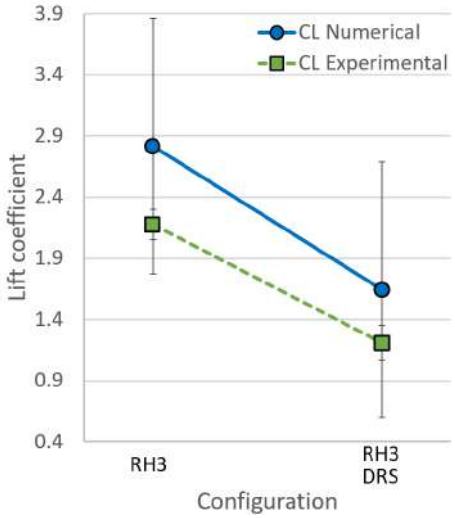

(a) Lift coefficient.

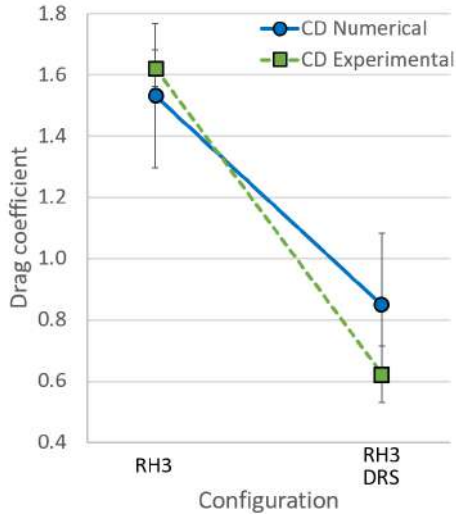

(b) Drag coefficient.

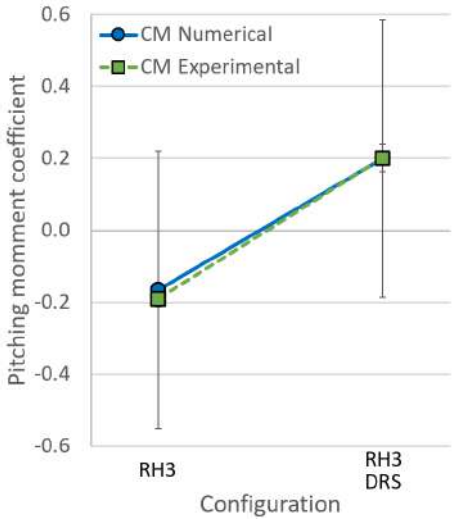

(c) Pitching moment coefficient.

Figure 13: DRS study aerodynamic loads.

Notoriously, the numerical simulation do not capture the drag coefficient (Fig. 13.(b)) high sensitivity registered during the experimental tests. Regarding the lift coefficient (Fig. 13.(a)), it presents the same behaviour for both configurations. Despite the higher sensitivity discrepancy noted on the drag coefficient, the lift coefficient difference remains approximately constant between the $RH3$ and $RH3 - DRS$ configurations.

Finally, the pitching moment coefficient (Fig. 13.(c)) highlights a considerable shift of the CoP between the $RH3$ and $RH3 - DRS$ configurations. During the experimental tests, the CoP of the $RH3$ configuration was located behind the attachment point ($C_M < 0$) and it shifted forwards with the $RH3 - DRS$ configuration ($C_M > 0$). In this case, the numerical simulation captured the behaviour of the experiments. This remark is corroborated by the pitch rotation experienced by the model in the wind tunnel, as illustrated in Fig. 14. However, CFD simulations did not reproduce any rotation since they work with rigid geometries. The model motion may be the source for some discrepancies registered in the results.

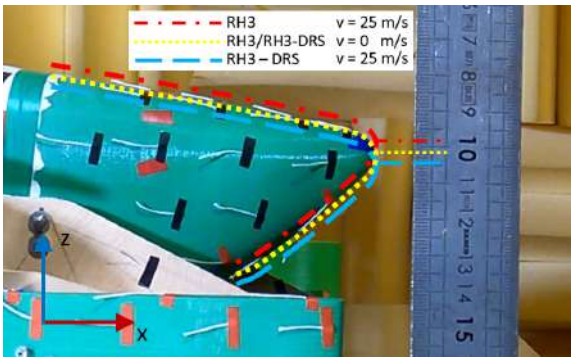

Figure 14: RH3-DRS configuration pitch rotation.

8. Conclusions

The main goal of this work was to manufacture and aerodynamically test a complete Formula Student vehicle in a wind tunnel to validate the computational fluid dynamics setup and simulations. To achieve it, several improvements were made to the Aeroacoustic wind tunnel in Aerospace Laboratory at IST that enabled a representative test of the FST10e model.

The hot film anemometry enabled the characterization of the wind tunnel airflow. Generally, experimental tests revealed a higher turbulence intensity in the entire test section than the numerical simulations. Inside the jet core, the turbulence intensity was approximately 2%. Overall, the numerical simulations presented the same trends as the wind tunnel airflow. However, the major difference was registered on the shear layers, where the free stream

affects the jet speed.

The numerical setup was developed to reproduce the model configurations tested in the wind tunnel. Modelling the entire wind tunnel nozzle as well as its test section revealed essential to define the initial requirements and constraints for the model itself and its positioning within the test section. The mesh convergence study presented a relatively low numerical error, 5.8% for the lift coefficient (C_L) and 4.3% for the drag coefficient (C_D). Yet, it revealed also the high uncertainties affecting the numerical setup. Moreover, the experimental uncertainties presented are considerably lower than the numerical ones.

One of the major marks of this thesis was the manufacture of a complete formula student model. Despite some geometry simplifications, the 1/3 scale FST10e model was faithful to the real prototype. Moreover, almost all simplifications were applied to the numerical setup to be as realistic as possible.

The high uncertainties did not enable a quantitative evaluation of the aerodynamic loads. However, a qualitative evaluation revealed that, generally, the numerical simulations captured the experimental trends. For instance, in the DRS study, the numerical simulation captured the C_L and C_M experimental sensitivities, while the numerical C_D sensitivity presented just a slight difference.

The wool tufts attached to the model surfaces enabled the visualization of airflow separation and turbulence zones. However, the numerical simulations presented some discrepancies with the tufts behaviour. The car presented 3D, mix transverse and longitudinal flow separations, which were difficult to evaluate using just tufts. Finally, the front wing tufts behaviour revealed that the flow that reached the car was already turbulent. Thus, the transition model used did not reproduce the wind tunnel flow visualization. Not using one proved to be beneficial to get a better match with the wind tunnel airflow.

Despite capturing the wind tunnel results trends and physics, the CFD simulations still need time investment and more testing to provide accurate data. They did not present an exact recreation of the wind tunnel as several components had to be suppressed. Moreover, CFD simulated a rigid body which did not match the experimental model behaviour. However, they proved to be useful in assessing how the geometry changes affect the aerodynamic performance of the car.

References

[1] History of formula student. Accessed: Oct 2021. url: https://www.imeche.org/events/formula-student/about-formula-student/history-of-formula-student.

[2] G. Hatton. Tech explained: Formula student aerodynamics. Racecar Engineering. Accessed: Oct 2021. url: https://www.racecar-engineering.com/articles/tech-explained-formula-student-aerodynamics.

[3] B. Rembold. 3D flow measurement in the wind tunnel - a formula student case study. AirShaper. Accessed: Oct 2021. url: https://airshaper.com/blog/3d-flow-measurement-formula-student.

[4] Smoke and tufts. Accessed: Nov 2021. url: https://www.grc.nasa.gov/www/k-12/airplane/tunvsmoke.html.

[5] M. Gonzalez, J. M. Ezquerro, V. Lapuerta, A. Laveron, and J. Rodriguez. *Components of a Wind Tunnel Balance: Design and Calibration*, chapter 7. IntechOpen, November 2011. doi: 10.5772/21095.

[6] O. Reynolds. On the dynamical theory of incompressible viscous fluids and the determination of the criterion. *Proceedings of the Royal Society of London. Series A: Mathematical and Physical Sciences*, 1995. doi: 10.1098/rspa.1995.0116.

[7] F. R. Menter. Two-equation eddy-viscosity turbulence models for engineering applications. *Aiaa Journal - AIAA J*, 32:1598–1605, 1994. doi: 10.2514/3.12149.

[8] X. Zheng, C. Liu, F. Liu, and C.-I. Yang. Turbulent transition simulation using the k – ω model. *International Journal for Numerical Methods in Engineering*, 42(5):907–926, 1998. doi: 10.1002/(SICI)1097-0207(19980715)42:5¡907::AID-NME393¿3.0.CO;2-T.

[9] L. Eça and M. Hoekstra. A procedure for the estimation of the numerical uncertainty of CFD calculations based on grid refinement studies. *Journal of Computational Physics*, 262:104–130, April 2014. doi: 10.1016/j.jcp.2014.01.006.

[10] J. B. Barlow, W. H. Rae, and A. Pope. *Low Speed Wind Tunnel Testing*. New York : Wiley, February 1999.

[11] A. Oliveira. Design, construction, calibration and testing of a wind tunnel force balance. Master's thesis, Instituto Superior Técnico, September 2020.